© 2024. Published by The Company of Biologists Ltd.
This is an Open Access article distributed under the terms of the Creative Commons Attribution License http://creativecommons.org/licenses/by /4.0), which permits unrestricted use, distribution and reproduction in any medium provided that the original work is properly attributed

Chloride transporter ClC-7 is essential for phagocytic clearance by microglia

Harini Iyer[*,‡], William S. Talbot[*]

Department of Developmental Biology, Stanford University School of Medicine, Stanford CA 94305, USA

[*]Corresponding authors: hrn.iyer@gmail.com; william.talbot@stanford.edu
[‡]Present address: Department of Biosciences, Rice University, Houston TX 77005

SUMMARY STATEMENT

Microglia, brain-resident macrophages, require the endolysosomal chloride transporter ClC-7 for effective clearance of debris.

ABSTRACT

Microglia, professional phagocytic cells of the brain, rely upon the appropriate activation of lysosomes to execute their immune and clearance functions. Lysosomal activity is, in turn, modulated by a complex network of over 200 membrane and accessory proteins that relay extracellular cues to these key degradation centers. The ClC-7 chloride-proton antiporter is localized to the endolysosomal compartments and mutations in *clcn7* lead to osteopetrosis and neurodegeneration. Although the functions of ClC-7 have been extensively investigated in osteoclasts and neurons, its role in microglia in vivo remains largely unexamined. Here we show that microglia and embryonic macrophages in *clcn7* mutants cannot effectively process extracellular debris in the form of apoptotic cells and beta-amyloid. Despite these functional defects, microglia develop normally in *clcn7* mutants and display normal expression of endosomal and lysosomal markers. We also find that mutants for *ostm1,* which encodes the beta-subunit of ClC-7, have a phenotype strikingly similar to that of *clcn7.* Together, our observations uncover a previously unappreciated role of ClC-7 in microglia and contribute to the understanding of the neurodegenerative phenotypes that accompany mutations in this channel.

Journal of Cell Science • Accepted manuscript

INTRODUCTION

Ion channels and transporters play a pivotal role in maintaining cellular and tissue homeostasis by controlling osmosis and cell volume, maintaining the appropriate pH of cellular organelles, and regulating membrane potential (Li et al., 2019). Lysosomes, as nutrient and stress sensors of the cell, especially rely on ion channels and transporters to transduce rapidly changing environmental and metabolic signals (Kendall and Holian, 2021). Furthermore, as highly acidic organelles of the cell, lysosomes and lysosomal activity are acutely sensitive to fluctuations in the ion balance (Riederer et al., 2023). The importance of ion flux to lysosomal function is underscored by observations showing that disrupted activity of ion channels and transporters leads to defects in degradation and recycling by lysosomes (Kendall and Holian, 2021). For example, Mucolipidosis Type IV, a lysosomal storage disorder, results from mutations in the calcium channel *TRPML1* (Dong et al., 2008). In addition, mutations in *TCIRG1* (vacuolar-H^+-ATPase) and *CLC-7* (Chloride channel-7) lead to Autosomal Recessive Osteopetrosis due to aberrant lysosomal activity in osteoclasts and consequent defects in bone resorption (Kornak et al., 2001; Susani et al., 2004).

Microglia, as the primary phagocytic cells of the central nervous system, depend on lysosomal activity to execute their surveillance and clearance functions (Holtman et al., 2015; Majumdar et al., 2007; Plaza-Zabala et al., 2017; Sole-Domenech et al., 2016). In addition, core microglial activities, including proliferation, migration, phagocytosis, and release of cytokines depend on the proper regulation of ion flux (Kettenmann et al., 2011). For instance, calcium transporters in microglia influence migration, ramified morphology, and podosome formation in these cells; sodium and potassium channels direct migration, volume regulation, and reactive oxygen species production by microglia; and chloride channels influence the membrane potential, phagocytosis, filopodia formation, and production of inflammatory cytokines by microglia (Furtner et al., 2007; Hines et al., 2009; Milton et al., 2008; Newell and Schlichter, 2005; Novarino et al., 2004). Aberrant expression of these channels in microglia has been implicated in neuropathic pain, ischemic stroke, traumatic brain injury, and most commonly, in neurodegenerative conditions associated with aging, including Alzheimer's disease and Parkinson's disease (Izquierdo et al., 2019).

Intracellular chloride levels are tightly regulated by chloride channels, including cystic fibrosis transmembrane regulator (CFTR) and the CLC family of chloride channels and chloride-proton antiporters (Chakraborty et al., 2017). CLC proteins have vital roles in regulating electrical

Journal of Cell Science • Accepted manuscript

excitability and maintaining the lumenal pH of subcellular compartments (Bose et al., 2021). Furthermore, these proteins localize to distinct compartments of the endolysosomal system, and mutations in the *CLC* family lead to lysosomal storage and processing defects (Chen et al., 2020; Pressey et al., 2010). In addition, mutations in *clcn7*, and its beta subunit *ostm1*, also lead to osteopetrosis, severe retinal degeneration, and neurodegeneration (Kasper et al., 2005). Although the functions of ClC-7 and Ostm1 have been widely investigated in osteoclasts (bone macrophages) and neurons (Bose et al., 2021; Kornak et al., 2001), their functions in microglia during development remain largely unexamined. Here we show that microglia display an inability to effectively clear apoptotic and neuronal debris in zebrafish *clcn7* mutants. In addition, embryonic macrophages and microglia in *clcn7* mutants are unable to process exogenous substrates, including bacteria and beta-amyloid peptide (1-42). Despite these functional deficits, microglia and embryonic macrophages develop normally in *clcn7* mutants, display normal expression of the markers of late endosomes and lysosomes, and respond appropriately to a variety of chemotactic cues. Our results uncover the role of ClC-7 in microglia and provide a new understanding of ClC-7-mediated neurodegeneration.

RESULTS AND DISCUSSION

Microglia in *clcn7* and *ostm1* mutants show reduced accumulation of neutral red

To examine the functions of *clcn7* and *ostm1* in microglia, we generated zebrafish mutants for these genes using CRISPR-Cas9. The *clcn7* mutants (*st167*) carry a 22 bp deletion in exon 1, leading to an early stop codon in the coding sequence (Fig. S1A). The *ostm1* mutation (*st168*) is a 5 bp deletion in exon 5 (Fig. S1B). Neutral red is a vital dye that is widely used to label microglia in zebrafish (Herbomel et al., 2001). We found that microglia in both *clcn7* and *ostm1* mutants showed sparse neutral red labeling (Figs. 1A and 1B). Notably, some *clcn7* and *ostm1* mutants displayed small neutral red punctae in the midbrain (Figs. 1A and 1B). These mutant phenotypes co-segregated with their respective lesions (numbers given in the legend to Fig. 1). In addition, co-injection of Cas9 and three different sgRNAs targeting other genomic regions in the *clcn7* locus caused a similar reduction in neutral red labeling in F0 CRISPR-injected animals (Fig. S2A). Neutral red dye is red below pH 6.8 and yellow between 6.8 and 8.0, so the disruption in *clcn7* and *ostm1* mutants could reflect changes in pH or the loss of microglia.

To establish whether microglia are present in *clcn7* and *ostm1* mutants, we used alternative methods for labeling microglia. Previous research in zebrafish has shown that microglia express

Journal of Cell Science • Accepted manuscript

apoeb in microglia starting at approximately 3 dpf (Peri and Nusslein-Volhard, 2008). Using in situ hybridization for *apoeb,* we found that *clcn7* and *ostm1* mutants display normal numbers and morphology of microglia (Fig. 1C). ClC-7 is a known target of the Microphthalmia-associated transcription factor (MiTF) family, and members of this protein family have gene dosage-dependent effects (Iyer et al., 2022). However, we found that microglia in *clcn7* and *ostm1* heterozygotes appeared similar to microglia in the wildtype siblings using both neutral red assay and *apoeb* in situ hybridization (Figs 1A-1C). We also used the *mpeg1:GFP* transgene, which drives GFP expression in cells of the macrophage lineage (Ellett et al., 2011), to visualize both microglia and embryonic macrophages. We found that cells of the macrophage lineage, including microglia (Fig. 1D) and peripheral macrophages in the head, yolk, and tail regions (Fig. S2B) appeared normal in *clcn7* mutant larvae. Humans carrying a gain-of-function mutation in *CLCN7* show delayed myelination in the corpus callosum (Nicoli et al., 2019). To examine a marker of myelinating glia, we performed in situ hybridization for *myelin basic protein* (*mbp*) and found that *mbp* expression in *clcn7* and *ostm1* mutants appeared comparable to heterozygotes (Fig. S2C). Thus, mutations in *clcn7* and *ostm1* lead to strikingly similar phenotypes with reduced accumulation of neutral red in microglia, which could indicate a disruption in microglial pH or efferocytosis (Demy et al., 2020).

Markers of late endosomes and lysosomes appear normal in *clcn7* mutants

Having established that mutants lacking ClC-7 and Ostm1 have similar phenotypes in microglia, we decided to focus on *clcn7* mutants to elucidate the functions of this ion channel in cells of the macrophage lineage. Although ubiquitously expressed, ClC-7 is the only member of the ClC family that localizes to late endosomes and lysosomes (Brandt and Jentsch, 1995). Furthermore, other groups have shown that mutation in *clcn7* can lead to the accumulation of electron-dense cytoplasmic material in neurons resembling lipofuscinosis (Kasper et al., 2005), suggesting possible defects in the endolysosomal pathway. To examine late endosomes and lysosomes in *clcn7* mutants, we used the previously generated transgenic zebrafish lines, *mpeg1:mCherry-Rab7* and *mpeg1:LAMP1-mCherry* (Iyer et al., 2022). These fusion proteins, driven by the *mpeg1* regulatory sequences, label late endosomes and lysosomes in cells of the macrophage lineage respectively. Our live microscopy analysis revealed that expression of both mCherry-Rab7 and LAMP1-mCherry appeared comparable in *clcn7* mutants and controls (Figs. 2A and 2B), indicating that these fusion proteins are normally expressed in *clcn7* mutants. To further investigate lysosomes in *clcn7* mutants, we used LysoTracker Red, which is a dye that accumulates in acidic compartments of cells and has previously been used to label lysosomal

Journal of Cell Science • Accepted manuscript

compartments of microglia in zebrafish (Shen et al., 2016). We found that both the area and intensity of LysoTracker Red punctae were normal in *clcn7* mutants (Fig. 2C). Consistent with our prior observations that the loss of *ostm1* leads to a phenotype strikingly similar to that of *clcn7* mutants, we found that *ostm1* mutants also exhibit normal staining by LysoTracker Red (Fig. S3A). Together, these observations demonstrate that markers of late endosomes and lysosomes appear to be normal in *clcn7* mutants.

Microglia in *clcn7* mutants are unable to effectively degrade endogenous debris

It was recently shown that loss of ClC-7 is required for degradation by phagolysosomes in bone marrow-derived macrophages (Wu et al., 2023). As the primary phagocytic cells of the central nervous system, microglia perform several critical functions for brain homeostasis and function, including clearing apoptotic debris, keeping neuronal progenitor numbers in check, and eliminating misfolded proteins (Matcovitch-Natan et al., 2016; Sierra et al., 2010; Tremblay et al., 2011; Zhan et al., 2014). We proceeded to systematically examine each of these functions of microglia in *clcn7* mutants. First, we performed TUNEL assay to visualize apoptotic debris clearance in the brain. Whereas *clcn7* heterozygotes had some TUNEL$^+$ punctae inside microglia, the intensity of TUNEL$^+$ punctae colocalizing with microglia was significantly greater in *clcn7* mutants (Fig. 3A). This observation indicates that microglia in *clcn7* mutants can effectively detect and ingest apoptotic debris but are apparently unable to effectively degrade the ingested apoptotic material. In addition to the TUNEL assay, we performed Acridine Orange staining (Tucker and Lardelli, 2007) and found that the number of Acridine Orange punctae in the head, eye, and tail regions of *clcn7* mutants was comparable to the staining in wildtype siblings (Fig. S3B), thus indicating that global apoptosis was normal in *clcn7* mutants.

In addition to their role as scavengers of apoptotic debris, microglia also regulate the number of neural precursor cells and sculpt neural circuits by pruning synapses (Cunningham et al., 2013; Hoshiko et al., 2012; Miyamoto et al., 2016; Pont-Lezica et al., 2014; Schafer et al., 2012; Squarzoni et al., 2014). We used the *NBT:DsRed* transgene to visualize the uptake and clearance of neuronal debris by microglia via live imaging. The analysis revealed a marked accumulation of neuronal debris inside the microglia of *clcn7* mutants (Figs. 3B-3E). Once again, to account for off-target effects, we used a combination of guide RNAs targeting three additional loci in the coding sequence of *clcn7* to confirm that microglia are unable to effectively process neuronal debris particles in *clcn7* CRISPR-injected F0 animals (Fig. S4A). To test the extent to which embryonic macrophages in *clcn7* mutants can effectively respond to a variety of

Journal of Cell Science • Accepted manuscript

chemotactic cues, we performed tail fin injury of zebrafish larvae and examined the macrophage response. Following injury, the macrophage response follows the early migration of neutrophils to the wound site (Mathias et al., 2009). We therefore examined the presence of macrophages at the wound site at 12 hours post-injury. We found that macrophages in *clcn7* wildtype siblings, heterozygotes, and mutants exhibited similar responses to injury (Fig. S4B), indicating that macrophages in *clcn7* can effectively sense injury cues. Collectively, these observations establish that microglia in *clcn7* mutants can effectively sense both apoptotic and live cellular debris but are unable to degrade the ingested material.

Exogenous debris is not efficiently cleared by embryonic macrophages and microglia in *clcn7* mutants

Next, we wanted to test the ability of embryonic macrophages and microglia to degrade exogenous substrates in *clcn7* mutants. First, we challenged peripheral embryonic macrophages with *E. coli* Texas Red (Fig. 4A) by injecting these microbial debris particles into the ducts of Cuvier of zebrafish larvae. Macrophages in both *clcn7* heterozygotes and mutants actively phagocytose *E. coli* particles and become activated and amoeboid in the process. However, the intensity of Texas Red punctae inside the macrophages of *clcn7* mutants was significantly greater compared to *clcn7* heterozygotes (Fig. 4A), indicating a greater accumulation of microbial debris inside the macrophages of *clcn7* mutants relative to heterozygotes. Next, to induce sterile inflammation, we injected Zymosan A into the midbrain ventricles of zebrafish larvae and found that the microglial response to inflammatory stress in *clcn7* mutants is similar to that in the heterozygotes (Fig. 4B). It was previously reported that PTU treatment leads to elevated autophagy in zebrafish larvae (Chen et al., 2021). In addition to ensuring that wildtype, heterozygotes, and mutant larvae were maintained under identical conditions in all our experiments, we also performed Zymosan A injection into the ducts of Cuvier in larvae not treated with PTU. We chose to examine the peripheral innate immune response because, in the absence of PTU treatment, the high density of pigment cells in the dorsal skin hinders the visualization of microglia. We found that the response of macrophages in *clcn7* mutants was comparable to that of controls (Fig. S4C).

Lastly, it has previously been shown that the degradation of amyloid fibrils in Alzheimer's disease required the delivery of ClC-7 to the lysosomes (Lee et al., 2020; Majumdar et al., 2011), and inefficient degradation of amyloid plaques by microglia in Alzheimer's disease is at least in part due to abnormal lysosomal acidification (Lee et al., 2020; Majumdar et al., 2007).

Journal of Cell Science • Accepted manuscript

To test the ability of microglia to effectively degrade the amyloid peptide in vivo, we injected beta-amyloid (1-42)-HiLyte Fluor 555 into the midbrain of zebrafish larvae. We found an increased accumulation of beta-amyloid particles within the microglia of *clcn7* mutants compared to heterozygotes (Fig. 4C). Together, our observations demonstrate that cells of the macrophage lineage exhibit reduced capacity to degrade endogenous as well as exogenous substrates. Future experiments will help illuminate if the accumulation of debris inside microglia and macrophages in *clcn7* mutants is due to a complete or partial loss of degradative function and explore mechanisms through which the clearance capabilities can be restored.

The molecular mechanism through which ClC-7 and chloride levels regulate the activity of lysosomes remains unclear. Although the prevailing model suggests that ClC-7 is a Cl^-/H^+ exchanger (Graves et al., 2008; Ishida et al., 2013; Leray et al., 2022; Mindell, 2012; Weinert et al., 2010), multiple lines of evidence indicate that lysosomal pH is normal in *clcn7* as well as *ostm1* mutants (Jentsch and Pusch, 2018; Kasper et al., 2005; Kornak et al., 2001). Furthermore, whereas disruption of lysosomal pH has been extensively reported in several mammalian cell culture models of lysosomal storage disorders (Bach et al., 1999; Holopainen et al., 2001; Sillence, 2013), recent evidence indicates that the drop in chloride concentration in these diseases may be significantly greater relative to the concomitant decrease in proton concentrations (Chakraborty et al., 2017). These observations, along with ours, further underscore the importance of chloride transport for lysosomal function even though the lumenal pH of lysosomes may be independent of chloride transport in at least some instances.

SUMMARY

The surveillance, clearance, and phagocytic capabilities of microglia are intimately linked to the appropriate activation and function of lysosomes. Multiple ion channels on the lysosomal membrane act in concert with one another to achieve a unique ionic microenvironment inside lysosomes (Kendall and Holian, 2021; Kettenmann et al., 2011). The delicate balance of ions within lysosomes is in turn crucial for the regulation of the pH, proteolytic activity, and processing capacity of these critical organelles. Here we show that the chloride transporter, ClC-7, and its partner Ostm1, are essential for the normal function of microglia. In zebrafish *clcn7* mutants, we find that microglia are unable to degrade extracellular debris effectively. Our findings are concordant with recent studies in *C. elegans* showing that a reduction in chloride levels correlates with a diminished degradative capacity of lysosomes (Chakraborty et al.,

Journal of Cell Science • Accepted manuscript

2017). Our data highlight the importance of chloride channel activity for the normal function of microglia. Our observations also have important implications for understanding the role of microglia in neurodegenerative phenotypes that accompany lysosomal storage disorders and autosomal recessive osteopetrosis.

MATERIALS AND METHODS

Zebrafish lines

Embryos from wildtype (TL or AB) strains and *Tg(mpeg:GFP)* were raised at 28.5 ºC. For all imaging experiments (except where noted), embryos were treated with 0.003% 1-phenyl-2-thiourea (PTU) in methylene blue embryo water to inhibit pigmentation, and anesthetization was done using .016% MS-222 (Tricaine) prior to experimental procedures. All animal protocols have been approved by the Stanford Institutional Animal Care and Use Committee.

CRISPR injections

sgRNAs targeting *clcn7* and *ostm1* were designed using CHOPCHOP. Oligonucleotides containing T7 binding site and the CRISPR sequence were annealed to tracrRNA template. Assembled oligonucleotides were transcribed using HiScribe T7 Quick (NEB, E2050S) kit. Following DNase treatment, the RNA was purified using mirVana miRNA isolation kit (Invitrogen, AM1561). An aliquot of the sgRNA eluate was run on agarose gel and quantified using nanodrop. CRISPR injections were performed at the 1-cell stage. The injection mix consisted of 300 ng/µl of Cas9 protein and 300 ng/µl of the sgRNA in Tris-HCl (pH 7.5). A small amount of phenol red was added to the mix to help with visualization during injection. The F1 progeny of F0-injected fish were verified for an out-of-frame insertion or deletion. Details of guideRNA and primers used: *clcn7* sgRNA sequence GGAGCGGTGTTCTCTCTCCGCGG; *clcn7* Forward Primer ACGGAAGTGCAACCCACAAC; *clcn7* Reverse Primer GGTCACGGGATTGCTTATGATTG. *clcn7* sgRNAs used for determining off-target effects: GGAGAACACCGCTGCTGAACGG, GGCTGCGGGAGTTTCTCAAGG, and GGCGGGAGTTTCTCAAGGCAGG. All three guide RNAs were co-injected with Cas9 to examine possible off-target effects in Figs. S2 and S4. *ostm1* sgRNA sequence GGTCTTCTATATCAATGCAGAGG; *ostm1* Forward Primer CTCTGCAAGGACTGCAAACCC; *ostm1* Reverse Primer CAGCTCTTTGGTGCTTACTTTGG.

Journal of Cell Science • Accepted manuscript

Neutral Red assay

Neutral Red was dissolved in distilled water to make a 2.5 mg/ml stock solution, which is stable at room temperature for several months. Staining using neutral red was done by treating larvae at 4 days post fertilization (dpf) with 5 µg/ml solution of neutral red in embryo water containing PTU for 3 hours. Animals were washed at least twice after 3 hours of incubation and left overnight in embryo water with PTU at 28.5 ºC to wash out the dye. Anesthetization and mounting in 1.5% agarose were done approximately 24 hours post-neutral red treatment. The number of Neutral Red^{+} microglia was counted, and the image was acquired immediately after counting using Zeiss AxioCam HRc camera with the AxioVision software. All the genotyping and statistical analysis were done post-imaging.

in situ hybridization

apoe and *mbp* antisense probes were synthesized as previously described (Lyons et al., 2005; Shiau et al., 2013). In situ hybridization was performed using standard methods (Thisse and Thisse, 2008). Briefly, embryos at 4 dpf were fixed overnight in 4% paraformaldehyde, dehydrated overnight in 100% methanol, rehydrated in PBS-Triton X-100 and PBS, permeabilized using proteinase K at a dilution of 1:1000 for 1 hour, incubated overnight with antisense riboprobes at 65 ºC. Following washes in 2X and 0.2X SSC, and incubation in MAB block containing 10% normal sheep serum, animals were incubated overnight at 4 ºC in block solution containing 1:1000 dilution of anti-digoxigenin antibody conjugated to alkaline phosphatase. The following day, after at least six 20-minute washes in MAB-Triton X-100 buffer, animals were incubated in the development solution containing NBT (Roche, 11383213001) and BCIP (11383221001). Development was stopped at the same time for all samples in a single experiment by evaluating the strength of the signal in control animals. Animals were washed twice in PBS-Triton X-100, left in 100% ethanol overnight for destaining, and rehydrated in PBSTx. Animals were mounted in 100% glycerol and images were captured using Zeiss AxioCam HRc camera with the AxioVision software. All the genotyping and statistical analysis were done post-imaging.

Transgene constructs and injection

Plasmids expressing the transgenic constructs *Tg(mpeg:mCherry-Rab7; cmcl2:GFP)* or *Tg(mpeg:LAMP1b-mCherry; cmlc2:GFP)* were co-injected at 12-25 pg along with 50-100 pg of Tol2 transposase mRNA at 1-cell stage (Iyer et al., 2022). *Tg(cmlc2:GFP)* was used as the selection marker for mCherry-rab7 and LAMP1b-mCherry fusion constructs and imaging was

Journal of Cell Science • Accepted manuscript

performed following confirmation of *Tg(cmlc2:GFP)* expression at 4 dpf. All the genotyping and statistical analysis were done post-imaging.

LysoTracker Red assay

LysoTracker Red DND-99 (ThermoFisher, L7528) was dissolved in embryo water with PTU at 1:100 dilution. Larvae at 4 dpf were incubated in the LysoTracker Red solution for 30-45 minutes. After staining, larvae were washed in embryo water containing PTU for 30 minutes, with at least 3 washes approximately 8-10 minutes apart. Following anesthetization and mounting, images were acquired using Zeiss LSM confocal microscope. The same imaging parameters (laser power, zoom, gain etc.) were used for a single experiment, all genotyping was done post-imaging. The area and intensity of LysoTracker Red punctae were calculated using ImageJ.

TUNEL assay

Larvae were fixed at 4 dpf with 4% paraformaldehyde for 2 hours at room temperature. Fixed larvae were permeabilized using Proteinase K (ThermoFisher, 25530049) at a dilution of 1:1000 for 30 minutes and post-fixed using 4% paraformaldehyde for 20 minutes at room temperature. Larvae were incubated in blocking solution (1% DMSO, 1% donkey serum, 1% BSA, 0.7% Triton X-100 in 1X PBS) for 2 hours at room temperature and incubated in blocking solution with anti-GFP antibody (1:500, Abcam, ab6658) overnight at 4 ºC. Following 6 10-minute washes in 1X PBS with 0.8% Triton X-100, larvae were incubated in block solution with 1:500 donkey anti-goat AlexaFluor 488 or 594 for 2 hours at room temperature, followed by 6 10-minute washes in 1X PBS with 0.8% Triton X-100. Larvae were incubated in 1:10 dilution of in situ cell death detection kit solution (Roche, SKU 12156792910) (10 µl enzyme solution with 90 µl label solution) and incubated at 37 ºC in the dark for 2 hours. Following washes with 1X PBS with 0.8% Triton X-100 overnight, animals were mounted in 2% agarose and imaged. Following imaging, the intensity of TUNEL punctae inside microglia was calculated using ImageJ. Genotyping and statistical analysis were done post-imaging.

Acridine Orange assay

Zebrafish larvae at 4 dpf were incubated in 5 µg/ml Acridine Orange (Sigma A9231) solution for 45 minutes. Larvae were washed in embryo water containing PTU for 45 minutes, with at least 3 washes approximately 10-15 minutes apart. Following anesthetization, all larvae were mounted

Journal of Cell Science • Accepted manuscript

laterally, and images were acquired using Zeiss LSM confocal microscope. The number of AO^+ punctae in the head, eyes, and tail were counted and all genotyping was done post-imaging.

Tail fin injury assay

Animals at 4 dpf were anesthetized and the tip of the tail fin was cut using a new scalpel ensuring approximately the same size of incision in all animals. Larvae were allowed to recover in embryo water. 12 hours post-injury, animals were mounted in 1.5% agarose with anesthetic. The number of macrophages at the site of injury (regenerated fin tissue and blastema) was counted and imaging was done using a 20X objective using Zeiss LSM Confocal microscope. Genotyping and statistical analysis were done post-imaging.

Neuronal debris quantitation

Larvae expressing *NBT:DsRed* and *mpeg:GFP* transgenes were imaged at 10X and 20X magnification using a Zeiss LSM Confocal microscope. Following imaging, the intensity of DsRed punctae inside microglia in the midline of the animal was calculated using ImageJ. All the genotyping and statistical analysis were done post-imaging.

***E. coli* Texas Red injection and imaging**

E. coli Texas Red (ThermoFisher E2863, 20 mg/ml in 1X PBS) injection was performed at 4 dpf by injecting 1 nl of the microbial suspension into the yolk of anesthetized larvae (Benard et al., 2012). Larvae were allowed to recover for 1 hour, anesthetized, mounted in 1.5% agarose, and imaged at 4 dpf using a Zeiss LSM Confocal microscope. Following imaging, the intensity of Texas Red punctae inside the tail macrophages was calculated using ImageJ. All the genotyping and statistical analysis were done post-imaging.

Zymosan A injection and imaging

Zymosan A (Sigma A4250, 1% in 1X PBS) injection was performed at 5 dpf by injecting 1 nl of the solution into the ventricles of the midbrain or optic tectum. Larvae were incubated for 2 hours, anesthetized, mounted in 1.5% agarose, and imaged using a Zeiss LSM Confocal microscope. Uninjected controls were incubated under the same conditions. All the genotyping and statistical analysis were done post-imaging.

Journal of Cell Science • Accepted manuscript

Beta-amyloid (1-42) injection and imaging

Beta-amyloid (1-42) HiLyte-Fluor555 (Anaspec, AS-60480-01) was reconstituted by adding 100 µl of 1% NH_4OH to 1 mg β-Amyloid and the stock was diluted to 1 mg/ml in 1X PBS. Injections were performed at 5 dpf by injecting 1 nl of the β-Amyloid suspension into each hemisphere of the midbrain of anesthetized larvae. Larvae were allowed to recover for 24 hours, anesthetized, mounted in 1.5% agarose, and imaged at 6 dpf using a Zeiss LSM Confocal microscope. Following imaging, the intensity of Fluor-555 punctae inside the microglia was calculated using ImageJ. All the genotyping and statistical analysis were done post-imaging.

ACKNOWLEDGMENTS

We would like to thank Dunya Shuman, Ranel Tuplano, and Vikram Mani for their contributions in the early phases of this project. We thank Tuky Reyes and Chenelle Hill for fish care, and we are grateful to Laura Pisani at the Stanford Center for Innovation in In vivo Imaging for her input on micro-CT scanning. We thank Raluca Nicoli and May Malicdan from NIH/NHGRI for generously sharing the CLCN7 plasmid. The Graphical Abstract was created using Biorender.

COMPETING INTERESTS

No competing interests declared.

FUNDING

H.I. was funded through a Developmental Project Award from Stanford Alzheimer's Disease Research Center and National Institute on Aging as well as a Postdoctoral Fellowship (A2021011F) from BrightFocus Foundation. W.S.T. was funded through National Institutes of Health grant R35NS111584. W.S.T. is the Mary and Dr. Salim Shelby Professor and a Kennedy-Grossman Fellow in Human Biology at Stanford University.

DATA AVAILABILITY

All relevant data can be found within the article and its supplementary information.

Journal of Cell Science • Accepted manuscript

REFERENCES

Bach, G., Chen, C. S. and Pagano, R. E. (1999). Elevated lysosomal pH in Mucolipidosis type IV cells. *Clin Chim Acta* **280**, 173-9.

Benard, E. L., van der Sar, A. M., Ellett, F., Lieschke, G. J., Spaink, H. P. and Meijer, A. H. (2012). Infection of zebrafish embryos with intracellular bacterial pathogens. *J Vis Exp*.

Bose, S., He, H. and Stauber, T. (2021). Neurodegeneration Upon Dysfunction of Endosomal/Lysosomal CLC Chloride Transporters. *Front Cell Dev Biol* **9**, 639231.

Brandt, S. and Jentsch, T. J. (1995). ClC-6 and ClC-7 are two novel broadly expressed members of the CLC chloride channel family. *FEBS Lett* **377**, 15-20.

Chakraborty, K., Leung, K. and Krishnan, Y. (2017). High lumenal chloride in the lysosome is critical for lysosome function. *Elife* **6**.

Chen, X. K., Kwan, J. S., Chang, R. C. and Ma, A. C. (2021). 1-phenyl 2-thiourea (PTU) activates autophagy in zebrafish embryos. *Autophagy* **17**, 1222-1231.

Chen, Z., Luciani, A., Mateos, J. M., Barmettler, G., Giles, R. H., Neuhauss, S. C. F. and Devuyst, O. (2020). Transgenic zebrafish modeling low-molecular-weight proteinuria and lysosomal storage diseases. *Kidney Int* **97**, 1150-1163.

Cunningham, C. L., Martinez-Cerdeno, V. and Noctor, S. C. (2013). Microglia regulate the number of neural precursor cells in the developing cerebral cortex. *J Neurosci* **33**, 4216-33.

Demy, D. L., Carrere, M., Noche, R., Tauzin, M., Le Bris, M., Baek, C., Leshchiner, I., Goessling, W. and Herbomel, P. (2020). The cationic amino acid exporter Slc7a7 is induced and vital in zebrafish tissue macrophages with sustained efferocytic activity. *J Cell Sci* **133**.

Dong, X. P., Cheng, X., Mills, E., Delling, M., Wang, F., Kurz, T. and Xu, H. (2008). The type IV mucolipidosis-associated protein TRPML1 is an endolysosomal iron release channel. *Nature* **455**, 992-6.

Ellett, F., Pase, L., Hayman, J. W., Andrianopoulos, A. and Lieschke, G. J. (2011). mpeg1 promoter transgenes direct macrophage-lineage expression in zebrafish. *Blood* **117**, e49-56.

Furtner, T., Zierler, S. and Kerschbaum, H. H. (2007). Blockade of chloride channels suppresses engulfment of microspheres in the microglial cell line, BV-2. *Brain Res* **1184**, 1-9.

Journal of Cell Science • Accepted manuscript

Graves, A. R., Curran, P. K., Smith, C. L. and Mindell, J. A. (2008). The Cl-/H+ antiporter ClC-7 is the primary chloride permeation pathway in lysosomes. *Nature* **453**, 788-92.

Herbomel, P., Thisse, B. and Thisse, C. (2001). Zebrafish early macrophages colonize cephalic mesenchyme and developing brain, retina, and epidermis through a M-CSF receptor-dependent invasive process. *Dev Biol* **238**, 274-88.

Hines, D. J., Hines, R. M., Mulligan, S. J. and Macvicar, B. A. (2009). Microglia processes block the spread of damage in the brain and require functional chloride channels. *Glia* **57**, 1610-8.

Holopainen, J. M., Saarikoski, J., Kinnunen, P. K. and Jarvela, I. (2001). Elevated lysosomal pH in neuronal ceroid lipofuscinoses (NCLs). *Eur J Biochem* **268**, 5851-6.

Holtman, I. R., Raj, D. D., Miller, J. A., Schaafsma, W., Yin, Z., Brouwer, N., Wes, P. D., Moller, T., Orre, M., Kamphuis, W. et al. (2015). Induction of a common microglia gene expression signature by aging and neurodegenerative conditions: a co-expression meta-analysis. *Acta Neuropathol Commun* **3**, 31.

Hoshiko, M., Arnoux, I., Avignone, E., Yamamoto, N. and Audinat, E. (2012). Deficiency of the microglial receptor CX3CR1 impairs postnatal functional development of thalamocortical synapses in the barrel cortex. *J Neurosci* **32**, 15106-11.

Ishida, Y., Nayak, S., Mindell, J. A. and Grabe, M. (2013). A model of lysosomal pH regulation. *J Gen Physiol* **141**, 705-20.

Iyer, H., Shen, K., Meireles, A. M. and Talbot, W. S. (2022). A lysosomal regulatory circuit essential for the development and function of microglia. *Sci Adv* **8**, eabp8321.

Izquierdo, P., Attwell, D. and Madry, C. (2019). Ion Channels and Receptors as Determinants of Microglial Function. *Trends Neurosci* **42**, 278-292.

Jentsch, T. J. and Pusch, M. (2018). CLC Chloride Channels and Transporters: Structure, Function, Physiology, and Disease. *Physiol Rev* **98**, 1493-1590.

Kasper, D., Planells-Cases, R., Fuhrmann, J. C., Scheel, O., Zeitz, O., Ruether, K., Schmitt, A., Poet, M., Steinfeld, R., Schweizer, M. et al. (2005). Loss of the chloride channel ClC-7 leads to lysosomal storage disease and neurodegeneration. *EMBO J* **24**, 1079-91.

Kendall, R. L. and Holian, A. (2021). The role of lysosomal ion channels in lysosome dysfunction. *Inhal Toxicol* **33**, 41-54.

Journal of Cell Science • Accepted manuscript

Kettenmann, H., Hanisch, U. K., Noda, M. and Verkhratsky, A. (2011). Physiology of microglia. *Physiol Rev* **91**, 461-553.

Kornak, U., Kasper, D., Bosl, M. R., Kaiser, E., Schweizer, M., Schulz, A., Friedrich, W., Delling, G. and Jentsch, T. J. (2001). Loss of the ClC-7 chloride channel leads to osteopetrosis in mice and man. *Cell* **104**, 205-15.

Lee, J. H., Wolfe, D. M., Darji, S., McBrayer, M. K., Colacurcio, D. J., Kumar, A., Stavrides, P., Mohan, P. S. and Nixon, R. A. (2020). beta2-adrenergic Agonists Rescue Lysosome Acidification and Function in PSEN1 Deficiency by Reversing Defective ER-to-lysosome Delivery of ClC-7. *J Mol Biol* **432**, 2633-2650.

Leray, X., Hilton, J. K., Nwangwu, K., Becerril, A., Mikusevic, V., Fitzgerald, G., Amin, A., Weston, M. R. and Mindell, J. A. (2022). Tonic inhibition of the chloride/proton antiporter ClC-7 by PI(3,5)P2 is crucial for lysosomal pH maintenance. *Elife* **11**.

Li, P., Gu, M. and Xu, H. (2019). Lysosomal Ion Channels as Decoders of Cellular Signals. *Trends Biochem Sci* **44**, 110-124.

Lyons, D. A., Pogoda, H. M., Voas, M. G., Woods, I. G., Diamond, B., Nix, R., Arana, N., Jacobs, J. and Talbot, W. S. (2005). erbb3 and erbb2 are essential for schwann cell migration and myelination in zebrafish. *Curr Biol* **15**, 513-24.

Majumdar, A., Capetillo-Zarate, E., Cruz, D., Gouras, G. K. and Maxfield, F. R. (2011). Degradation of Alzheimer's amyloid fibrils by microglia requires delivery of ClC-7 to lysosomes. *Mol Biol Cell* **22**, 1664-76.

Majumdar, A., Cruz, D., Asamoah, N., Buxbaum, A., Sohar, I., Lobel, P. and Maxfield, F. R. (2007). Activation of microglia acidifies lysosomes and leads to degradation of Alzheimer amyloid fibrils. *Mol Biol Cell* **18**, 1490-6.

Matcovitch-Natan, O., Winter, D. R., Giladi, A., Vargas Aguilar, S., Spinrad, A., Sarrazin, S., Ben-Yehuda, H., David, E., Zelada Gonzalez, F., Perrin, P. et al. (2016). Microglia development follows a stepwise program to regulate brain homeostasis. *Science* **353**, aad8670.

Mathias, J. R., Walters, K. B. and Huttenlocher, A. (2009). Neutrophil motility in vivo using zebrafish. *Methods Mol Biol* **571**, 151-66.

Journal of Cell Science • Accepted manuscript

Milton, R. H., Abeti, R., Averaimo, S., DeBiasi, S., Vitellaro, L., Jiang, L., Curmi, P. M., Breit, S. N., Duchen, M. R. and Mazzanti, M. (2008). CLIC1 function is required for beta-amyloid-induced generation of reactive oxygen species by microglia. *J Neurosci* **28**, 11488-99.

Mindell, J. A. (2012). Lysosomal acidification mechanisms. *Annu Rev Physiol* **74**, 69-86.

Miyamoto, A., Wake, H., Ishikawa, A. W., Eto, K., Shibata, K., Murakoshi, H., Koizumi, S., Moorhouse, A. J., Yoshimura, Y. and Nabekura, J. (2016). Microglia contact induces synapse formation in developing somatosensory cortex. *Nat Commun* **7**, 12540.

Newell, E. W. and Schlichter, L. C. (2005). Integration of K+ and Cl- currents regulate steady-state and dynamic membrane potentials in cultured rat microglia. *J Physiol* **567**, 869-90.

Nicoli, E. R., Weston, M. R., Hackbarth, M., Becerril, A., Larson, A., Zein, W. M., Baker, P. R., 2nd, Burke, J. D., Dorward, H., Davids, M. et al. (2019). Lysosomal Storage and Albinism Due to Effects of a De Novo CLCN7 Variant on Lysosomal Acidification. *Am J Hum Genet* **104**, 1127-1138.

Novarino, G., Fabrizi, C., Tonini, R., Denti, M. A., Malchiodi-Albedi, F., Lauro, G. M., Sacchetti, B., Paradisi, S., Ferroni, A., Curmi, P. M. et al. (2004). Involvement of the intracellular ion channel CLIC1 in microglia-mediated beta-amyloid-induced neurotoxicity. *J Neurosci* **24**, 5322-30.

Peri, F. and Nusslein-Volhard, C. (2008). Live imaging of neuronal degradation by microglia reveals a role for v0-ATPase a1 in phagosomal fusion in vivo. *Cell* **133**, 916-27.

Plaza-Zabala, A., Sierra-Torre, V. and Sierra, A. (2017). Autophagy and Microglia: Novel Partners in Neurodegeneration and Aging. *Int J Mol Sci* **18**.

Pont-Lezica, L., Beumer, W., Colasse, S., Drexhage, H., Versnel, M. and Bessis, A. (2014). Microglia shape corpus callosum axon tract fasciculation: functional impact of prenatal inflammation. *Eur J Neurosci* **39**, 1551-7.

Pressey, S. N., O'Donnell, K. J., Stauber, T., Fuhrmann, J. C., Tyynela, J., Jentsch, T. J. and Cooper, J. D. (2010). Distinct neuropathologic phenotypes after disrupting the chloride transport proteins ClC-6 or ClC-7/Ostm1. *J Neuropathol Exp Neurol* **69**, 1228-46.

Riederer, E., Cang, C. and Ren, D. (2023). Lysosomal Ion Channels: What Are They Good For and Are They Druggable Targets? *Annu Rev Pharmacol Toxicol* **63**, 19-41.

Journal of Cell Science • Accepted manuscript

Schafer, D. P., Lehrman, E. K., Kautzman, A. G., Koyama, R., Mardinly, A. R., Yamasaki, R., Ransohoff, R. M., Greenberg, M. E., Barres, B. A. and Stevens, B. (2012). Microglia sculpt postnatal neural circuits in an activity and complement-dependent manner. *Neuron* **74**, 691-705.

Shen, K., Sidik, H. and Talbot, W. S. (2016). The Rag-Ragulator Complex Regulates Lysosome Function and Phagocytic Flux in Microglia. *Cell Rep* **14**, 547-559.

Shiau, C. E., Monk, K. R., Joo, W. and Talbot, W. S. (2013). An anti-inflammatory NOD-like receptor is required for microglia development. *Cell Rep* **5**, 1342-52.

Sierra, A., Encinas, J. M., Deudero, J. J., Chancey, J. H., Enikolopov, G., Overstreet-Wadiche, L. S., Tsirka, S. E. and Maletic-Savatic, M. (2010). Microglia shape adult hippocampal neurogenesis through apoptosis-coupled phagocytosis. *Cell Stem Cell* **7**, 483-95.

Sillence, D. J. (2013). Glucosylceramide modulates endolysosomal pH in Gaucher disease. *Mol Genet Metab* **109**, 194-200.

Sole-Domenech, S., Cruz, D. L., Capetillo-Zarate, E. and Maxfield, F. R. (2016). The endocytic pathway in microglia during health, aging and Alzheimer's disease. *Ageing Res Rev* **32**, 89-103.

Squarzoni, P., Oller, G., Hoeffel, G., Pont-Lezica, L., Rostaing, P., Low, D., Bessis, A., Ginhoux, F. and Garel, S. (2014). Microglia modulate wiring of the embryonic forebrain. *Cell Rep* **8**, 1271-9.

Susani, L., Pangrazio, A., Sobacchi, C., Taranta, A., Mortier, G., Savarirayan, R., Villa, A., Orchard, P., Vezzoni, P., Albertini, A. et al. (2004). TCIRG1-dependent recessive osteopetrosis: mutation analysis, functional identification of the splicing defects, and in vitro rescue by U1 snRNA. *Hum Mutat* **24**, 225-35.

Thisse, C. and Thisse, B. (2008). High-resolution in situ hybridization to whole-mount zebrafish embryos. *Nat Protoc* **3**, 59-69.

Tremblay, M. E., Stevens, B., Sierra, A., Wake, H., Bessis, A. and Nimmerjahn, A. (2011). The role of microglia in the healthy brain. *J Neurosci* **31**, 16064-9.

Tucker, B. and Lardelli, M. (2007). A rapid apoptosis assay measuring relative acridine orange fluorescence in zebrafish embryos. *Zebrafish* **4**, 113-6.

Journal of Cell Science • Accepted manuscript

Weinert, S., Jabs, S., Supanchart, C., Schweizer, M., Gimber, N., Richter, M., Rademann, J., Stauber, T., Kornak, U. and Jentsch, T. J. (2010). Lysosomal pathology and osteopetrosis upon loss of H+-driven lysosomal Cl- accumulation. *Science* **328**, 1401-3.

Wu, J. Z., Zeziulia, M., Kwon, W., Jentsch, T. J., Grinstein, S. and Freeman, S. A. (2023). ClC-7 drives intraphagosomal chloride accumulation to support hydrolase activity and phagosome resolution. *J Cell Biol* **222**.

Zhan, Y., Paolicelli, R. C., Sforazzini, F., Weinhard, L., Bolasco, G., Pagani, F., Vyssotski, A. L., Bifone, A., Gozzi, A., Ragozzino, D. et al. (2014). Deficient neuron-microglia signaling results in impaired functional brain connectivity and social behavior. *Nat Neurosci* **17**, 400-6.

Journal of Cell Science • Accepted manuscript

Figures

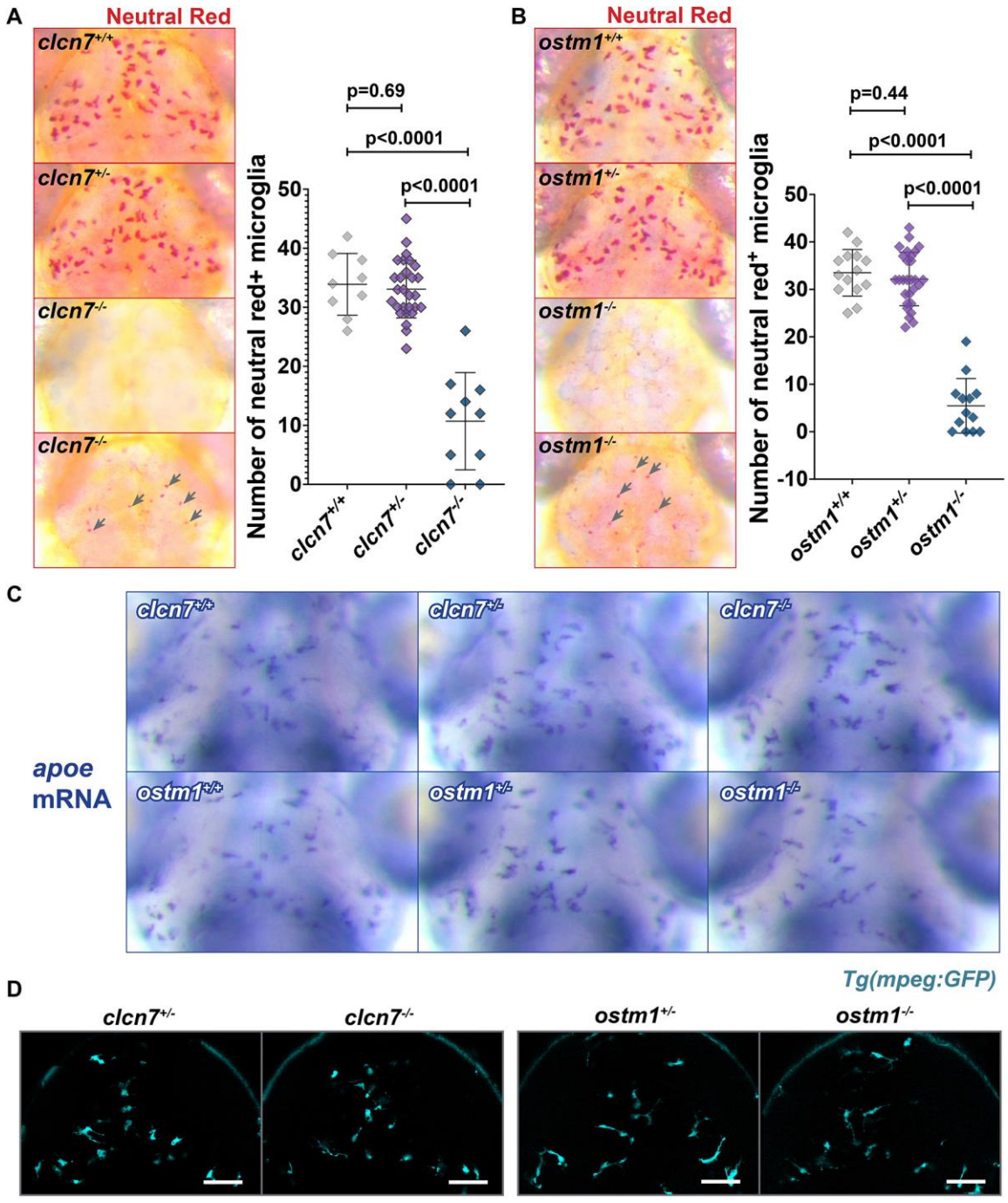


Fig. 1. Reduced neutral red staining in *clcn7* and *ostm1* mutants. Neutral red labeling revealed significantly fewer microglia labeled with this vital dye in **A.** *clcn7* and **B.** *ostm1* mutants. Some mutants displayed small neutral red punctae (grey arrows in A

Journal of Cell Science • Accepted manuscript

and B). These smaller neutral red punctae were included in the quantitation. *clcn7*$^{+/+}$: N=9, mean=33.9, SD=5.2, SEM=1.7. *clcn7*$^{+/-}$: N=28, mean=33.1, SD=4.9, SEM=1.0. *clcn7*$^{-/-}$: N=10, mean=10.7, SD=8.2, SEM=2.6. *ostm1*$^{+/+}$: N=14, mean=33.5, SD=4.9, SEM=1.3. *ostm1*$^{+/-}$: N=28, mean=32.2, SD=5.6, SEM=1.1. *ostm1*$^{-/-}$: N=13, mean=5.5, SD=5.8, SEM=1.6. Two-tailed unpaired t-test with Welch's correction was performed to calculate significance; graphs show mean with SD. **C.** *apoe* in situ hybridization showed that *clcn7* and *ostm1* mutants have normal numbers and morphology of microglia. **D.** Confocal microscopy confirmed that *mpeg1:GFP* expression is normal in *clcn7* and *ostm1* mutants. Images in A, B, and D are representative of at least 3 independent experiments. Scale bars, 50 μm.

Journal of Cell Science • Accepted manuscript

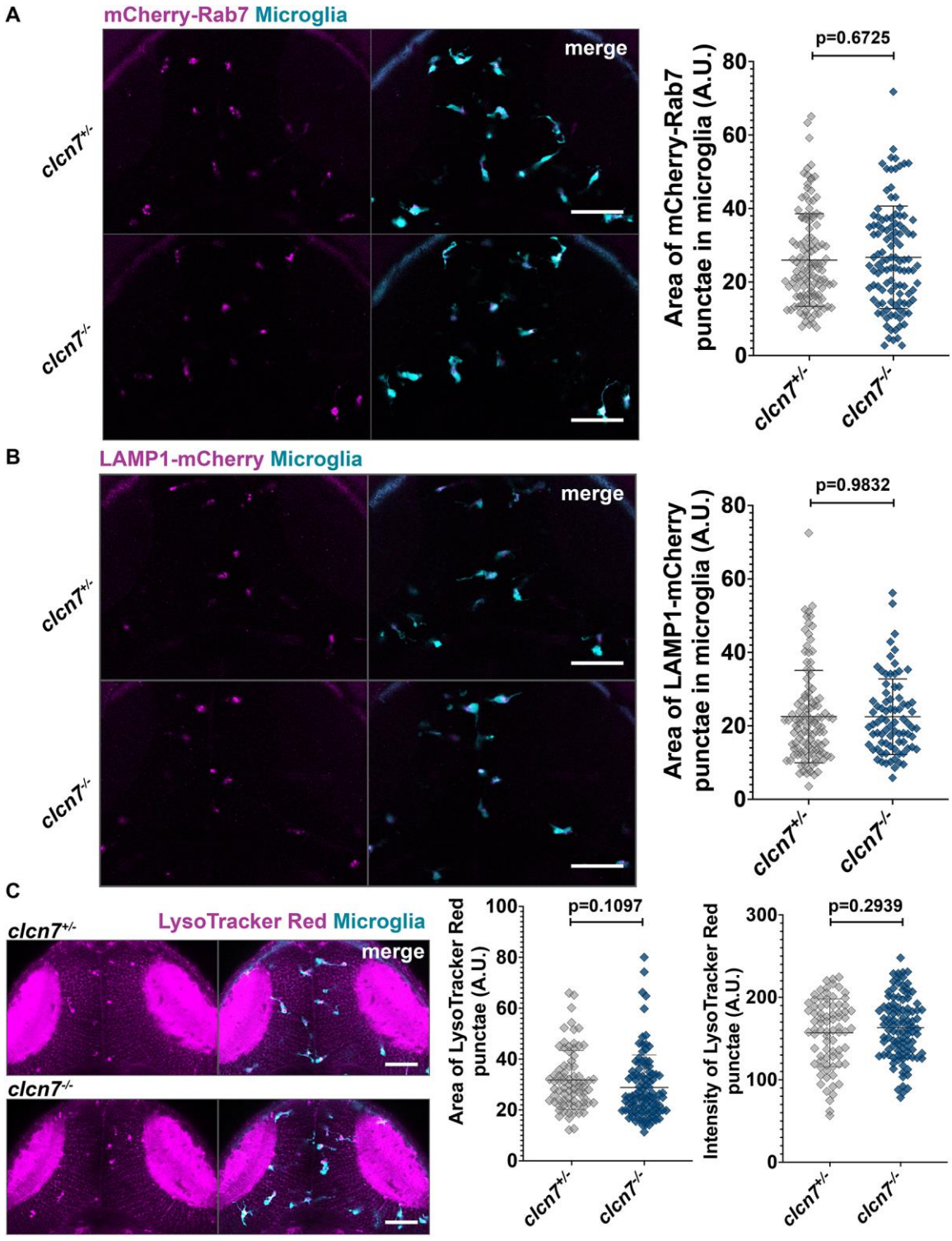


Fig. 2. Late endosomal and lysosomal compartments appear normal in *clcn7* mutants. Transgenic expression of **A.** *mCherry-Rab7* and **B.** *LAMP1b-mCherry* driven under the control of *mpeg1* regulatory sequences was similar in *clcn7* heterozygotes

Journal of Cell Science • Accepted manuscript

and mutants. *mCherry-Rab7; clcn7*$^{+/-}$: N=17, mean=26.0, SD=12.6, SEM=1.1. *mCherry-Rab7; clcn7*$^{-/-}$: N=8, mean=26.7, SD=14.0, SEM=1.3. *LAMP1b-mCherry; clcn7*$^{+/-}$: N=18, mean=22.5, SD=12.6, SEM=1.2. *LAMP1b-mCherry; clcn7*$^{-/-}$: N=8, mean=22.5, SD=10.3, SEM=1.2. **C.** Area and intensity of LysoTracker Red were similar *clcn7* heterozygotes and mutants. *clcn7*$^{+/-}$ area: N=14, mean=31.8, SD=11.6, SEM=1.3. *clcn7*$^{-/-}$ area: N=17, mean=28.8, SD=12.8, SEM=1.3. *clcn7*$^{+/-}$ intensity: N=14, mean=157, SD=41.1, SEM=4.7. *clcn7*$^{-/-}$ intensity: N=17, mean=163.3, SD=37.5, SEM=3.7. Two-tailed unpaired t-test with Welch's correction was performed to calculate significance; graphs show mean with SD. Images are representative of 2 independent experiments. All scale bars, 50 μm.

Journal of Cell Science • Accepted manuscript

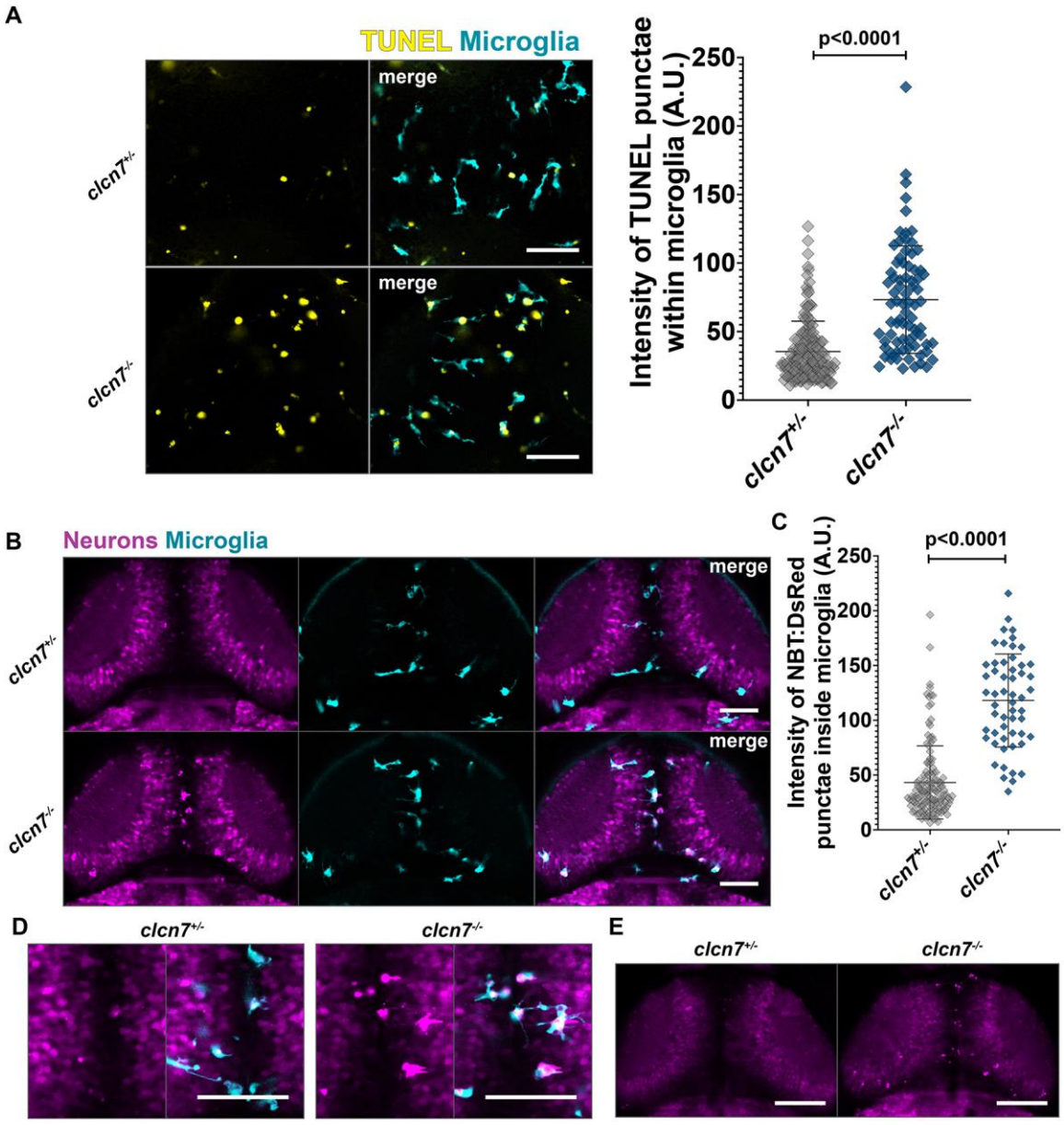


Fig. 3. Microglia are unable to effectively clear endogenous debris in *clcn7* mutants. A. TUNEL assay revealed a significantly greater intensity of apoptotic punctae inside the microglia of *clcn7* mutants (N=6, mean=73.3, SD=39.2, SEM=4.5) than in *clcn7* heterozygotes (N=12, mean=35.5, SD=22.2, SEM=1.8). **B.** Microglia in *clcn7* mutants show an accumulation of NBT:DsRed neuronal punctae. **C.** Intensity of DsRed punctae inside microglia was significantly greater in *clcn7* mutants (N=13, mean=118, SD=42.4, SEM=5.7) relative to *clcn7* heterozygotes (N=29, mean=43.2, SD=33.4,

Journal of Cell Science • Accepted manuscript

SEM=2.9) **D.** High magnification image showing accumulation of neuronal debris inside microglia. **E.** Low magnification image showing accumulation of NBT:DsRed punctae in the midbrain, where microglia are enriched. Two-tailed unpaired t-test with Welch's correction was performed to calculate the significance in all graphs; graphs show mean with SD. All scale bars, 50 μm.

Journal of Cell Science • Accepted manuscript

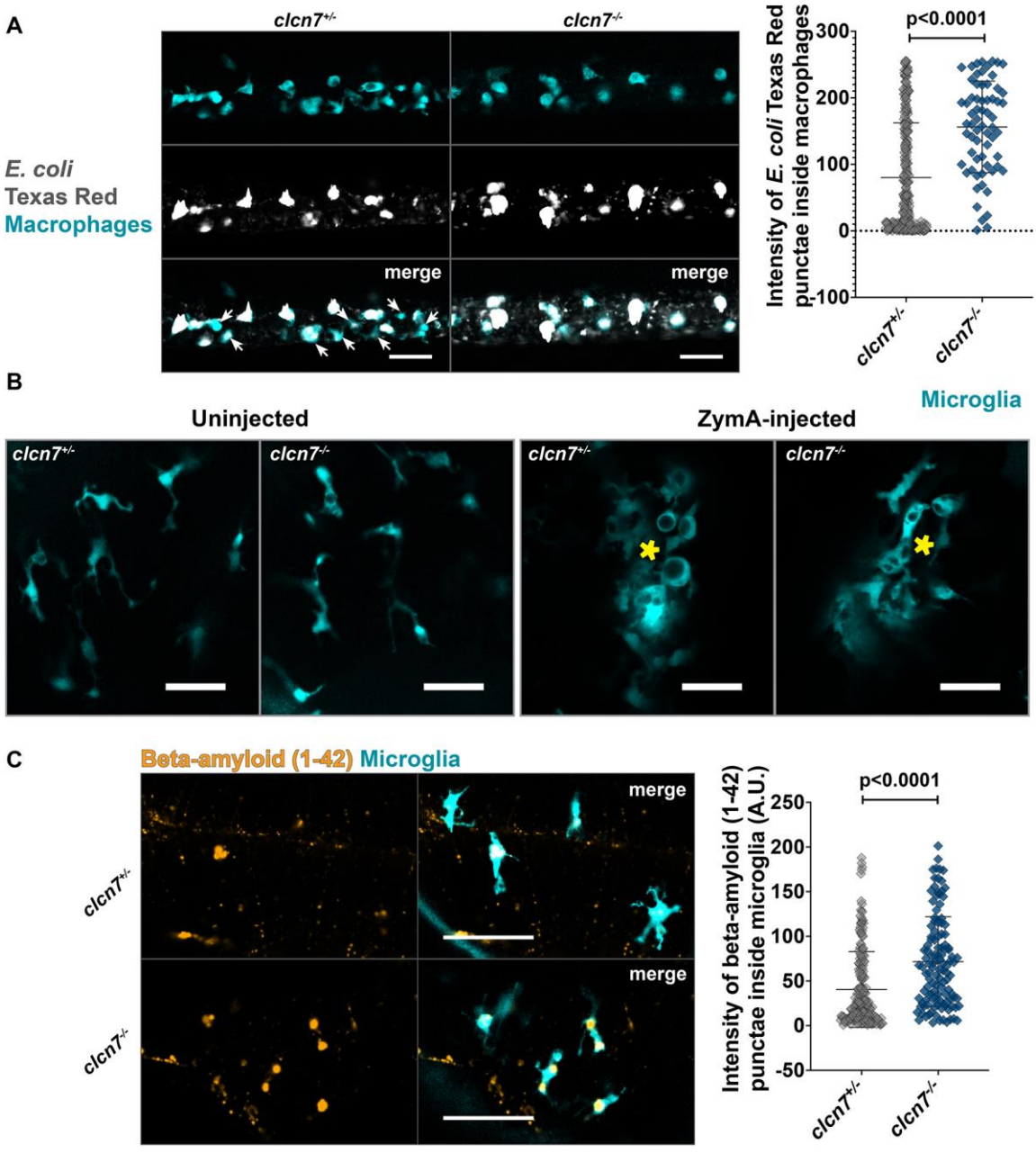


Fig. 4. Exogenous debris accumulates inside microglia and macrophages of *clcn7* mutants. A. *E. coli* Texas Red particles injected in the ducts of Cuvier accumulate inside peripheral macrophages. The intensity of Texas Red particles inside the macrophages is greater in *clcn7* mutants (N=8, mean=156.2, SD=68.8, SEM=8.5) than in *clcn7* heterozygotes (N=27, mean=80.2, SD=82.3, SEM=5.1). Arrows indicate macrophages containing little or no *E. coli* in control animals. Scale bars, 50 μm. **B.** Zymosan A injected into the midbrain of zebrafish larvae to observe microglia response.

Journal of Cell Science • Accepted manuscript

Microglia in *clcn7* mutants and heterozygotes respond similarly to inflammatory stress. Yellow asterisks mark the site of injection. Scale bars, 20 μm. **C.** Beta-amyloid (1-42) HiLyte Fluor-555 particles injected into the midbrain of zebrafish larvae accumulate inside the microglia of *clcn7* mutants (N=16, mean=71.7, SD=50.3, SEM=4.6) to a significantly greater extent than in *clcn7* heterozygotes (N=26, mean=40.5, SD=42.5, SEM=3.0). Scale bars, 50 μm. Two-tailed unpaired t-test with Welch's correction was performed to calculate the significance in all graphs; graphs show mean with SD.

Journal of Cell Science • Accepted manuscript

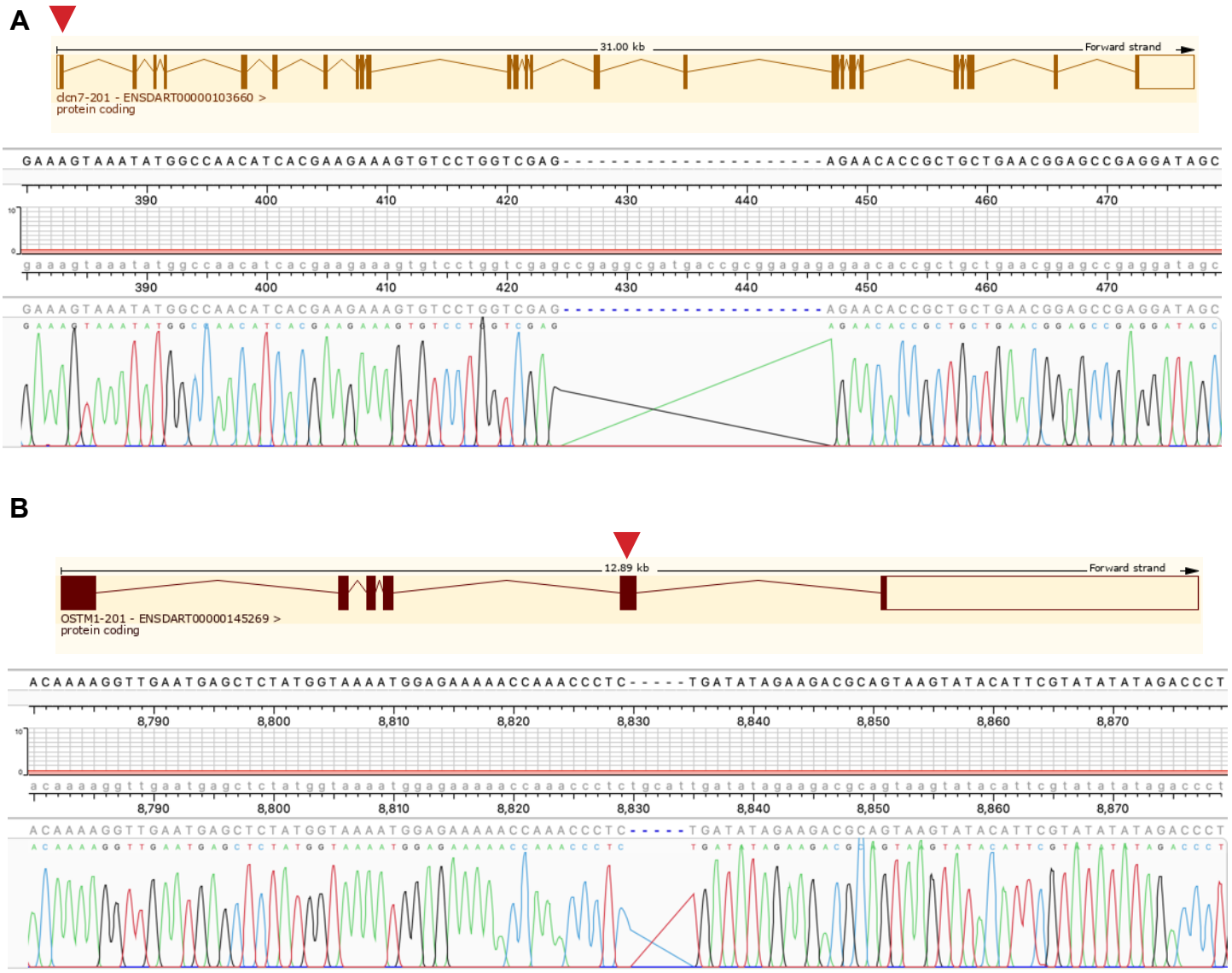
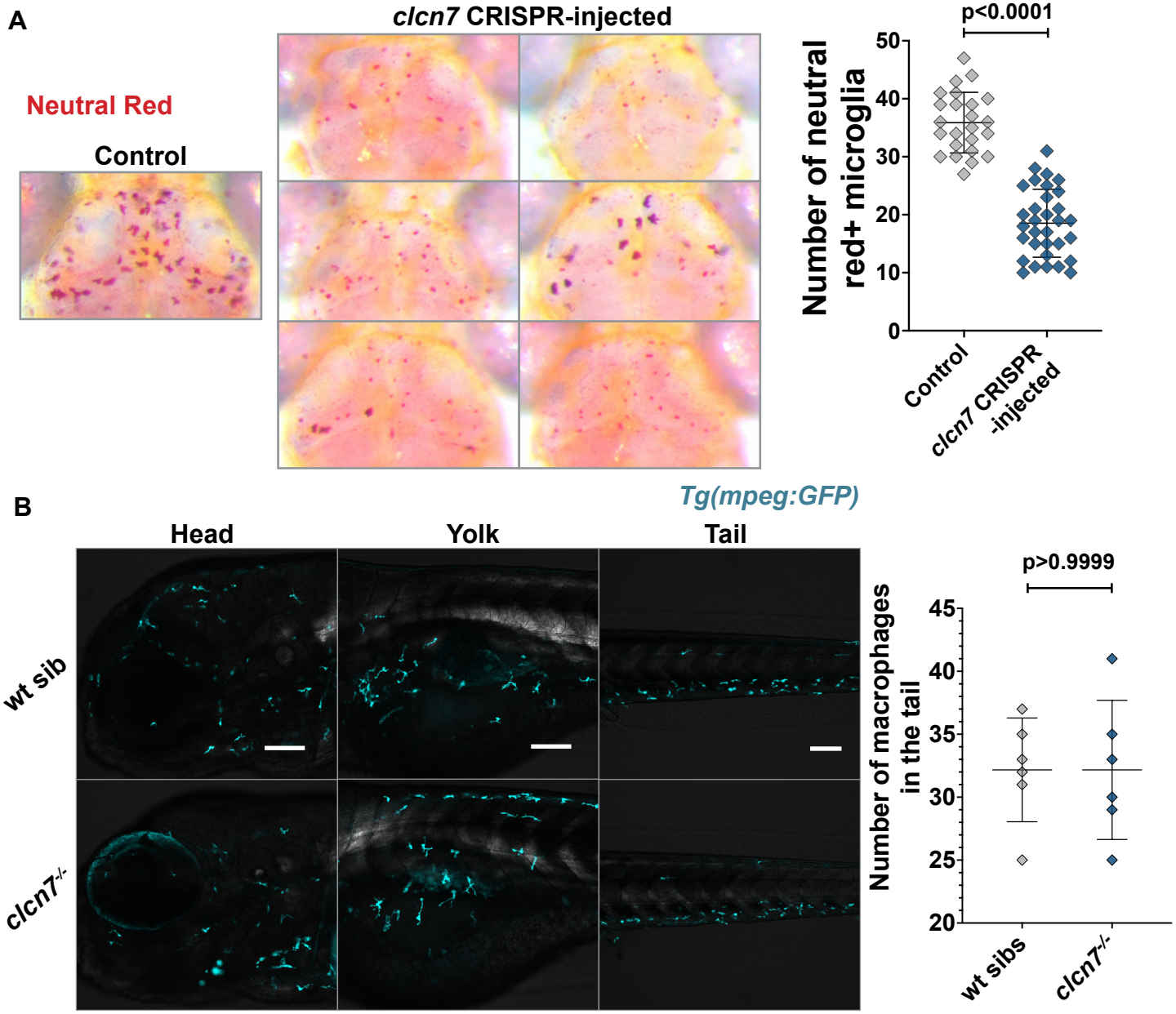


Fig. S1. Chromatograms showing the mutations in *clcn7* (st167) and *ostm1* (st168). A. *clcn7* mutants have a 22 bp deletion in exon 1 (arrowhead on gene structure at top). **B.** *ostm1* mutants have a 5 bp deletion in exon 5 (arrowhead on gene structure at top). These deletions introduce frameshift mutations and truncate the predicted proteins.

Journal of Cell Science • Supplementary information



Journal of Cell Science • Supplementary information

Fig. S2. A. Synthetic guide RNAs targeting different regions of the *clcn7* genomic locus were injected into one-cell zebrafish embryo, followed by neutral red staining at 4 days post fertilization. (Control: N=24, mean=35.9, SD=5.2, SEM=1.1. *clcn7* CRISPR-injected: N=32, mean=18.5, SD=5.9, SEM=1.0.) **B.** *mpeg1:GFP* expression showing that numbers of macrophages in the head, yolk, and tail regions of *clcn7* mutants are similar to wildtype siblings at 4 dpf. Scale bars, 100 μm. Tail macrophages: wildtype siblings N=6, mean=32.2, SD=4.1, SEM=1.7; *clcn7* mutants N=6, mean=32.2, SD=5.5, SEM=2.3. **A, B.** Two-tailed unpaired t-test with Welch's correction was performed to determine statistical significance; graph shows mean with SD. **C.** in situ hybridization showed similar expression of *mbp* in *clcn7* and *ostm1* heterozygotes and mutants at 5 dpf.

Journal of Cell Science • Supplementary information

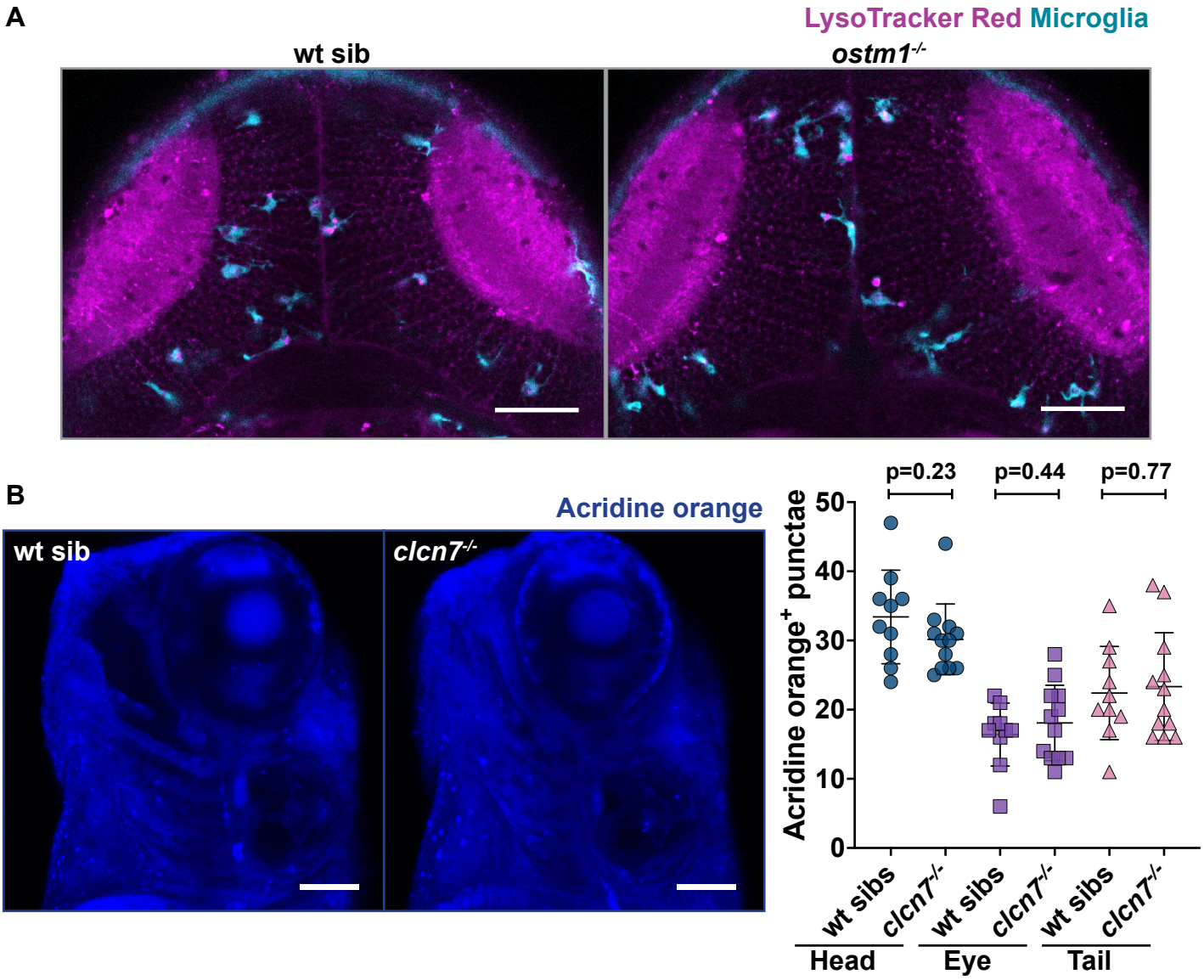
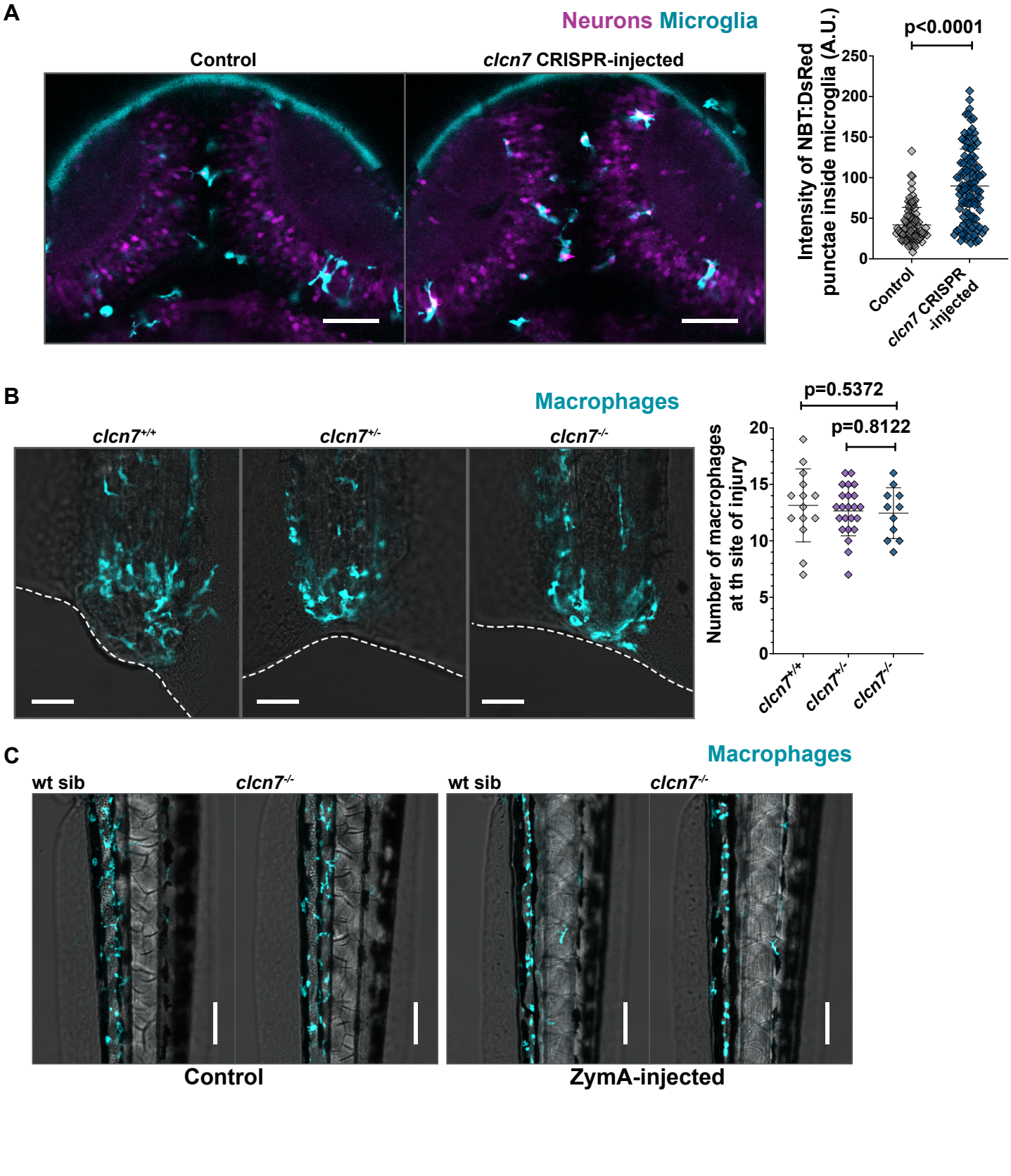


Fig. S3. A. LysoTracker Red labeling is comparable in *ostm1* mutants and wildtype siblings. **B.** Acridine orange labeling shows that the number of apoptotic cells were similar in *clcn7* mutants and their wildtype siblings in the head (wt sibs: N=10, mean=33.4, SD=6.8, SEM=2.1 and mutants: N=12, mean=30.2, SD=5.1, SEM=1.5), eye (wt sibs: N=10, mean=16.4, SD=4.6, SEM=1.4 and mutants: N=12, mean=18.1, SD=5.5, SEM=1.6), and tail (wt sibs: N=10, mean=22.4, SD=6.7, SEM=2.1 and mutants: N=12, mean=23.3, SD=7.8, SEM=2.3). All counts are from lateral mounts. Two-tailed unpaired t-test with Welch's correction was performed to calculate signi icance; graphs show mean with SD. All scale bars, 100 μm.

Journal of Cell Science • Supplementary information



Journal of Cell Science • Supplementary information

Fig. S4. A. Mosaic animals injected with *clcn7* CRISPRs targeting different genomic loci also show defects in neuronal debris clearance (control: N=33, mean=41.7, SD=21.7, SEM=2.2 and *clcn7* CRISPants: N=34, mean=89.8, SD=45.5, SEM=4.3). Scale bars, 50 μm. **B.** Embryonic macrophages in *clcn7* mutants effectively respond to peripheral injury effectively (*clcn7*$^{+/+}$: N=14, mean=13.1, SD=3.2, SEM=0.9. *clcn7*$^{+/-}$: N=23, mean=12.7, SD=2.2, SEM=0.5. *clcn7*$^{-/-}$: N=11; mean=12.5, SD=2.3, SEM=0.7). Scale bars, 50 μm. Two-tailed unpaired t-test with Welch's correction was performed to calculate significance; graphs show mean with SD. **C.** Macrophages in *clcn7* mutant embryos not treated with PTU and injected with ZymA respond similarly to macrophages in wildtype siblings. Scale bars, 100 μm.

Journal of Cell Science • Supplementary information